Journal of Cultural Heritage 72 (2025) 160–168

Contents lists available at ScienceDirect

Journal of Cultural Heritage

journal homepage: www.elsevier.com/locate/culher

Original article

Non-destructive examination of ancient vitreous materials from Southwest Asia: Synchrotron computed tomography at the BEATS beamline of SESAME

Gianluca Iori[a,b,*], Philipp Hans[a], Neva Maria Elisabetta Stucchi[c,d], Latif Ullah Khan[a], Abdellatif Saadaldin[e], Elena Possenti[f], Giulia Franceschin[c], Samah Al Khasoneh[g], Gian Luca Bonora[f], Gonca Dardeniz[h]

[a] SESAME – Synchrotron-light for Experimental Science and Applications in the Middle East, Allan, Jordan
[b] Institute for Biomedical Engineering, ETH Zürich and University of Zürich, Zürich, Switzerland
[c] Center for Cultural Heritage Technologies (CCHT), Istituto Italiano di Tecnologia, Venice, Italy
[d] Department of Molecular Sciences and Nanosystems, Università Ca'Foscari Venezia, Venice, Italy
[e] Department of Mathematics, Faculty of Sciences, An-Najah National University, Nablus, Palestine
[f] Institute of Heritage Science, National Research Council, ISPC-CNR, Milan, Italy
[g] Sela for Training and Protection of Heritage, Wadi Musa, Petra, Jordan
[h] Istanbul University, Faculty of Letters, Department of Archaeology, Protohistory and Near Eastern Archaeology Section, Istanbul, Türkiye

ARTICLE INFO

Article history:
Received 10 October 2024
Accepted 28 January 2025

Keywords:
Glass
Faience
X-ray tomography
Phase-contrast imaging
Synchrotron radiation
Chemical mapping

ABSTRACT

The analysis of archaeological objects poses a set of challenges related to the fragility and uniqueness of the material and requires special non-invasive techniques. This article presents applications of Synchrotron X-ray Computed Tomography (SXCT) on archaeological vitreous materials, namely glass, faience, and Egyptian blue. Using five different case studies, we provide protocols developed at the beamline ID10-BEATS of SESAME (Jordan) to understand raw material, production, and degradation of vitreous assemblages from sub-mm to several cm in size. The use of high-resolution 3-dimensional X-ray imaging combined with phase-contrast generation allows to identify and differentiate ancient faience and pigment production technologies, quantify the severity and microstructure of glass corrosion, and assess the fracture and mechanical fragility of large artifacts and assemblies such as mosaics. The combination of SXCT with synchrotron X-ray fluorescence mapping and X-ray absorption near edge structure allows to examine complementary structural and chemical data of unique examples of the Southwest Asian cultural heritage. The availability of a SXCT facility at the heart of Southwest Asia facilitates and enhances the non-destructive examination and conservation of ancient vitreous materials of the region, proving the relevance of the technique for archaeologists, museums, and cultural heritage specialists.
© 2025 The Author(s). Published by Elsevier Masson SAS. This is an open access article under the CC BY license (http://creativecommons.org/licenses/by/4.0/)

1. Introduction

The examination of cultural heritage materials requires non-destructive techniques to preserve their integrity. Among the diverse array of such artifacts, vitreous materials (hereafter, VM) compose one of the most fragile groups. Ancient faience, Egyptian blue, and glass have all been synthetically produced from silica-based materials and colored with various metallic minerals, mostly copper oxides and carbonates. Ancient crafts' ability to play with the shape of VM and assortment in their color provides an alternative to the limitations (e.g., access, price) of natural raw materials like the valued stones, such as blue-colored lapis lazuli or orange- to brown-colored carnelian. The durable and vivid tones of Egyptian blue as pigment or the possibility to recycle glass provided ancient crafts with diverse uses of the materials. Consequently, VM stayed in use for millennia and established a significant repertoire of archaeological and museum collections. Central research questions when dealing with this type of material are 1) to understand the details of the production technologies and 2) to assess the alteration or degradation of the specimen, guiding conservation approaches.

* Corresponding author at: Institute for Biomedical Engineering, ETH Zürich and University of Zürich, Zürich, Switzerland.
E-mail addresses: giiori@ethz.ch, gianluca.iori@sesame.org.jo (G. Iori).

https://doi.org/10.1016/j.culher.2025.01.011
1296-2074/© 2025 The Author(s). Published by Elsevier Masson SAS. This is an open access article under the CC BY license (http://creativecommons.org/licenses/by/4.0/)

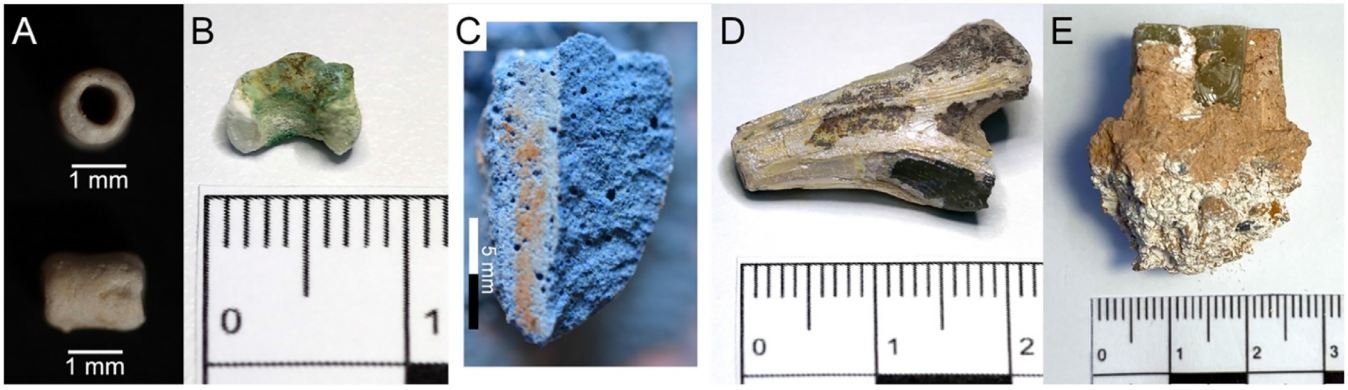

Fig. 1. Digital photographs of the samples used for this work. **A)** Faience microbead from grave 6.A of Adji Kui, southern Turkmenistan; **B)** Faience bead from Başur Höyük, eastern Türkiye; **C)** Egyptian blue sample from Van, Türkiye; **D)** Roman glass sample from Petra, Jordan; **E)** Replica of Roman mosaic with glass tesserae.

X-ray-based techniques provide a means to study the internal composition and structure of objects without destruction. X-ray Computed Tomography (XCT) employs X-ray radiation to generate 3-dimensional (3D) images of a body or specimen [1]. By using micro-focus X-ray sources and exploiting high geometrical magnification, modern laboratory micro-CT systems can detect features in the micrometer range. Previous studies have demonstrated the use of X-ray micro-CT for the analysis of historical glass beads from $<$1 mm to few centimeters in size [2–4]. Porosities, cracks, stratifications and material inhomogeneities product of bead manufacturing, resulting from the use of coloring agents or from corrosion proceeding from the glass surface were visualized with voxels (3D pixels) with a size between 2.6 µm and 75 µm. Synchrotron tomography beamlines exploit high-brilliance bremsstrahlung radiation emitted by relativistic electrons to perform XCT with resolution, sensitivity and speed superior to conventional micro-CT [5]. Despite a considerable body of literature reporting on the application of Synchrotron X-ray Computed Tomography (SXCT) to cultural heritage materials of different nature and dimensions [5–7], there is comparatively limited literature regarding the examination of VM. X-ray phase-contrast tomography, requiring a partially spatial coherent X-ray source, was used to verify the consolidation of cracked archeological glass [8]. Absorption-contrast SXCT with submicron voxel size could track the effects and progression of a consolidation treatment aimed at removal of manganese from historical stained glass [9]. SXCT with phase-contrast and voxel sizes of 1 µm and 2 µm was used to study deposits and multi-layer patina formations on the surface and within cavities of archaeological Roman glass [10], providing sensitivity and resolution superior to laboratory micro-CT [11].

In this work, we demonstrate the application of SXCT for the non-destructive examination of different types of VM. We regard the large volume of data produced by experiments and the lack of open and reproducible data analysis procedures as common obstacles that hinder the widespread use of SXCT. Consequently, we provide guidelines for the acquisition of SXCT scans and standard protocols guiding prospective users in the reconstruction and analysis of 3D images, and for the characterization of the internal microstructure of vitreous specimens. The focus is put on the capabilities of the new SXCT beamline BEATS of the SESAME synchrotron in Jordan, thereby revealing the availability and potential impact of the first SXCT imaging station in Southeast Asia and North Africa. Finally, we demonstrate how the combination of SXCT with other synchrotron analytical techniques such as X-ray fluorescence (XRF) mapping can further enhance the understanding of the origin and conservation state of VM, particularly glass.

2. Research aim

The objective of this study is to provide potential and experienced SXCT users with a comprehensive protocol for analyzing ancient VM using SXCT. We aim to demonstrate to scholars in the fields of archaeology, archaeological science, conservation, and museum studies the potential of SXCT for non-destructive examination of VM. The technique, which has been so far not available to museums and institutions in the geographical region of SESAME, is foreseen to become a vital non-invasive method for working with fragile and valuable artifacts.

Five case studies are selected based on specific archaeological questions shaped around different VM. Open-source protocols for SXCT scanning, image reconstruction, and data analysis tailored to the artifacts under investigation are provided. These pipelines can be adapted to specimens of different sizes and compositions.

3. Material and methods

3.1. Materials

The presented study investigates different VM collected from archaeological sites covering diverse landscapes and chronologies. Reflecting the fact that each archaeological object is unique, we present specimens that vary significantly in size, composition, condition, and fragility. The SXCT scanning approach is tailored accordingly.

Four archaeological samples and one archaeological replica are used in this study (Fig. 1). The archaeological samples include 1) a faience microbead from southern Turkmenistan (Fig. 1A), dated to the late 3rd millennium BCE, 2) a faience bead fragment (Fig. 1B) dated to 3100–2900 BCE, eastern Türkiye, 3) an Egyptian blue sample (Fig. 1C) dated to the 1st millennium BCE from eastern Türkiye, and 4) a Roman glass sample (Fig. 1D) from Petra, Jordan. The only replica refers to a Roman mosaic with glass tesserae (Fig. 1E) produced by the Scuola Mosaicisti del Friuli in Spilinbergo - Italy. The replica is included for the purpose of demonstrating 1) a SXCT scan modality for relatively large and dense objects, and 2) the non-destructive investigation of Roman mosaic glass production via SXCT. A description of each specimen and relevant archeological context is provided in Suppl. 1.

3.2. Synchrotron X-ray computed tomography (SXCT)

Tomographic images of all samples were collected at the SXCT beamline ID10-BEATS of SESAME. Tomography is a non-destructive

Table 1
List of samples, indicating the specimen size and the main parameters of the SXCT scan protocol. A detailed table of scan parameters is provided in Suppl. 2. SDD: Sample-Detector-Distance.

Sample	Size [mm^2]	Magnif.	Voxel size [µm]	Energy [keV]	SDD [mm]	No. Angles	Scan time
Faience microbead	1.2 × 1.8	10 ×	0.65	20	10	1800	1 h
		4 ×	1.63	20	10	1000	30 min
Faience bead	4 × 7	4 ×	1.63	30	15	1800	1 h
		2 ×	3.1	30	300	4000	11 min
Egyptian blue	8 × 15	2 ×	3.1	45	300	4000	6 min
Roman glass	15 × 25	1 ×	4.5	20	250	8000	10 min
Mosaic mockup	28 × 33	0.5 ×	13.65	69	900	8000	1 h

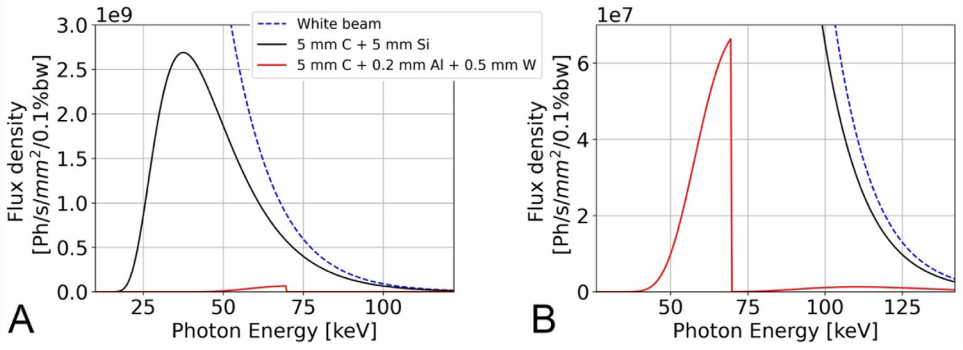

Fig. 2. A) X-ray photon flux density (number of X-ray photons per square millimeter and second) at the sample position of the ID10-BEATS SXCT beamline of SESAME. Filtered white beam configuration (black line, 36 keV peak energy) providing high photon flux and broadband energy spectrum. **B)** Detail of A showing the narrow-bandwidth, high-energy X-ray energy spectrum obtained by filtering the beam with 5 mm of carbon (C), 0.2 mm of aluminum (Al), and 0.5 mm of tungsten (W) (red line, 69 keV peak energy).

imaging technique based on the use of penetrating X-ray radiation to deliver virtual volume images of the specimen under investigation [1]. Typically, volume images are retrieved from a set of projection images covering a wide range of angular views based on the computational process of tomographic reconstruction. Widely available imaging modalities such as magnetic resonance imaging (MRI) and computed tomography (CT) with conventional X-ray sources can both attain 3D micrometric resolution, but the achievable contrast, spatial, and temporal resolution is limited. In contrast, the high brilliance and partial spatial coherence of synchrotron X-rays allow a drastic reduction of the time needed for high-resolution tomographic studies and boosting of contrast thanks to the use of phase-contrast enhancement [12].

ID-10 BEATS employs a dedicated wavelength shifter photon source, providing a hard X-ray probe with tunable energy up to 100 keV. Interchangeable X-ray detectors and a state-of-the-art data acquisition and processing facility allow routine scans with voxel sizes from 13 µm down to 0.65 µm, and visualization of volume images within minutes. The beamline instrumentation used for this work is described in detail in [13]. For SXCT scanning, all samples were mounted using custom holders and protective material such as light foam or parafilm wrapping. Table 1 shows the main SXCT scan parameters adopted for each experiment. The beamline's insertion device was operated at minimum gap (11.15 mm) and the front-end slits partially closed to generate a secondary source of enhanced spatial coherence as described in [14]. All scans of archeological specimens were performed with quasi-monochromatic X-rays using the beamline's double multilayer monochromator, reducing the total X-ray dose delivered to the sample. The scan energy was selected compromising between exposure time and visibility of features on radiographic projections. In particular, the ratio between the intensity of dark and bright areas of projection images was in the range between 0.1 and 0.5. Due to their longer attenuation length, large and dense specimens require the use of higher X-ray scan energy. For the Roman mosaic replica, a high-energy scan configuration was utilized by filtering the polychromatic beam (Fig. 2A) with 5 mm of glassy carbon (C), 0.2 mm of aluminum (Al), and 0.5 mm of tungsten (W). This delivered to the sample a beam with a relatively narrow bandwidth and peak energy of 69 keV (Fig. 2B). Due to low detector counts, 4 images were averaged for each projection for the Roman mosaic scan.

The distance between sample and detector was adjusted to favor propagation-based fringe formation and phase-contrast enhancement [15]. The selected distance increases with the scan energy and voxel size (Table 1). Different detectors based on scintillating screens and indirect visible light optics were used [13]. The magnification was chosen so that the entire specimen could be captured by the detector's field of view (FOV). For the faience bead and Roman glass scans, the FOV was extended horizontally by rotating the sample over 360°. For the Roman glass and mosaic mockup scans, the FOV was extended vertically, performing 3 and 5 scans at different sample heights, respectively.

3.3. Tomographic reconstruction

All SXCT images were reconstructed using TomoPy [16] through the web application Alrecon [17] following the protocol outlined in Table 2. The open-source Python reconstruction pipeline utilized for this work is open-source and available on GitHub and Zenodo [18]. A detailed description of the pipeline is provided in Suppl. 3. Propagation-based phase-contrast 3D images were generated by applying a phase-retrieval step before reconstruction [19]. This allows to generate image contrast based on the difference in the electron density of the constituent elements. In comparison to absorption-contrast, hard X-ray SXCT in phase-contrast mode can provide greater sensitivity to light elements [12,20].

3.4. Image processing and analysis

After reconstruction, all images were inspected and cropped using ImageJ [23]. 3D rendering and section views were created in

Table 2
Phase-contrast enhanced SXCT image reconstruction protocol. A detailed description of the pipeline is provided in Suppl. 3.

Step	Process	Description
1	Flat-field correction	For long scans or flat-field images collected at a different time of the scan, the flat-field intensity is normalized by the synchrotron storage ring current.
2	Stripe removal	Eliminate ring-shaped artifacts from reconstructed images using one of the approaches [21].
3	Phase retrieval	Retrieve phase shift from absorption projections with Paganin's method [19].
4	Tomographic reconstruction	Computed with the regridding reconstruction algorithm implementation of TomoPy [16,22].
5	Write TIFF stack to disk	Images can be converted to 8-bit format to reduce size.

Table 3
SXCT 3D image processing protocol. Details are provided in Suppl. 3.

Step	Process	Description
1	Axial scan stitching	Combine 3D volume of multiple scans performed at different sample heights
2	Crop region of interest (ROI)	Reduce image size for analysis
3	Background removal	See Suppl. 3 for details
4	Segmentation	
4.1	Whole sample mask	Generate a continuous mask of the sample body without holes. Isolate sample from background and surrounding material (e.g. lightweight foam or sample holder)
4.1.1	Down-sample greyscale image	Reduce image size for faster segmentation
4.1.2	Median filter	Smooth sharp image features (e.g. small pores)
4.1.3	Otsu thresholding	Segment dataset with single upper Otsu threshold [24]
4.1.4	Voids 3D filling	Remove holes from the segmented dataset
4.1.5	3D image open	Remove voxels protruding from the sample
4.1.6	Remove unconnected voxels	Keep only the largest object. Remove voxels not connected to the sample
4.2	Single compartments masks	Generate separate label images for the different phases present in the sample (incl. voids and background)
4.2.1a	K-means segmentation	Iterative algorithm that segments the data into clusters based on feature similarity minimizing an intra-cluster variance metric. The number of clusters and iterations are given by the user.
4.2.1b	Otsu thresholding (alternatively)	Segment compartments based on local image intensity. Several threshold values are calculated from the image intensity histogram with the Otsu approach depending on the number of phases in the sample.
4.2.2	Binary mask manipulation	As in steps 4.1.4, 4.1.5, 4.1.6
4.2.3	Manual mask correction	Manually remove remaining holes, portions of background, or protrusions
4.2.4	Watershed transform	Applied to voids mask to isolate touching pores
4.3	Pore masks	Intersect voids mask and each compartment mask (incl. whole sample) to obtain pore mask for each phase
5	Pore analysis	
5.1	Calculate porosity	The volume ratio between pore and individual compartment mask. Repeat for each compartment as well as for the whole sample
5.2	Generate pore multi-ROI	Generate a label image where each label corresponds to a single pore
5.3	Compute pore properties	Typical metrics: pore volume, max. Feret diameter, sphericity, aspect ratio, principal axis orientation
6	Compute local thickness	Allow quantitative rendering of the thickness of a sample region
7	Plot, export, and save results	

Dragonfly (Comet Technologies Canada Inc., Montreal, Canada). A quantitative 3D analysis of the internal porosity of the microbead and Egyptian blue samples was performed. Porosity and local thickness of the surface alteration layer on the Roman glass sample were quantified using open-source Python code [18]. Table 3 describes a generic protocol for volume image processing followed for microbead, Egyptian blue, and Roman glass samples. A detailed version of the Python image processing pipeline of Table 3 applied to the Roman glass specimen is described in Suppl. 3.

3.5. X-ray fluorescence (XRF) mapping and X-ray absorption near edge structure (XANES)

XRF mappings and XANES measurements were performed at the BM08-XAFS/XRF beamline of SESAME [25]. The XRF method was employed to obtain information about the specimen's elemental composition. Accessible elements are those heavier than sulfur, owing to the absorption of the emission lines of lighter elements in the air. The beamline's XRF mapping tool was employed to collect XRF maps in a step-by-step scanning mode, employing a KETEK Silicon Drift Detector (SDD) with a Digital X-ray Processor (DXP) by Mercury XIA LLC. The map's pixel size was 200 µm where the integration time was 2s.

XANES data were collected to probe the lead (Pb) distribution within the Roman glass sample at ultra-low concentrations. Pb L3-edge (13,035 eV) XANES data were collected from the top portion of the sample in fluorescence mode at room temperature. A double-crystal silicon (Si 111) monochromator was used to set the incoming X-ray energy. Incident and transmitted beam intensities were recorded by three ionization chambers, each filled with N_2/Ar (nitrogen-argon) gas mixtures at a total pressure of 1.0 bar, subsequently amplified by Stanford picoammeters. Energy calibration was done utilizing a lead (Pb) foil.

4. Results

4.1. Faience microbead

Fig. 3 shows phase-contrast SXCT images of the faience microbead. Adapting the detector magnification to the sample size allowed to obtain a 3D volume rendering (Fig. 3A) and virtual sections (Fig. 3B-C) of the entire specimen. Fig. 3B reveals the microstructure of the sample's body (BDY), which is characterized by the presence of fine-crushed, sharp-edged grains/fragments (possibly quartz), and binding matrix. The sharp-edged grains are bound together in a homogeneous, highly compact light grey glassy bind-

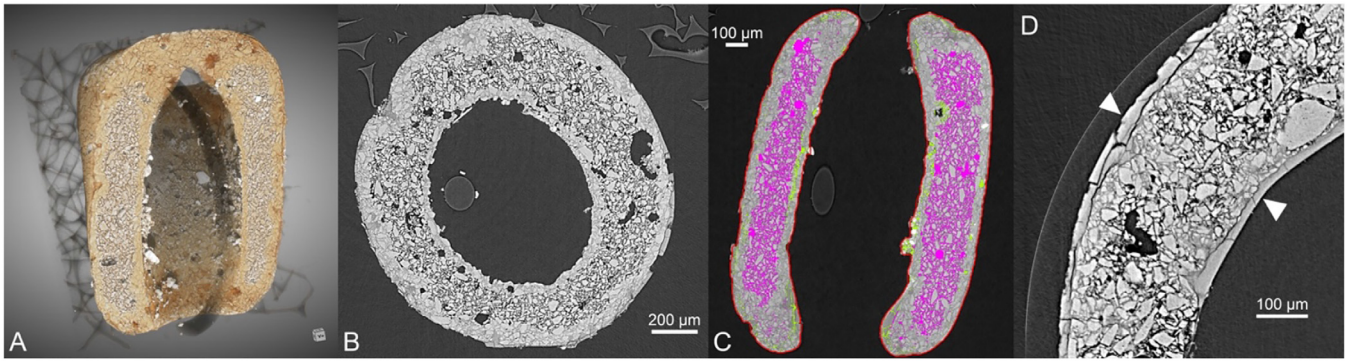

Fig. 3. **A)** 3D rendering; **B)** virtual cross-section from SXCT scan of the faience microbead. The plastic foam and thread used to mount the sample are visible. **C)** Longitudinal section showing porosities in the GLZ and core sample regions (light-green and magenta highlights, respectively). **D)** High-resolution detail of the microbead showing a clear separation between surface GLZ (arrowheads) and the sample interior.

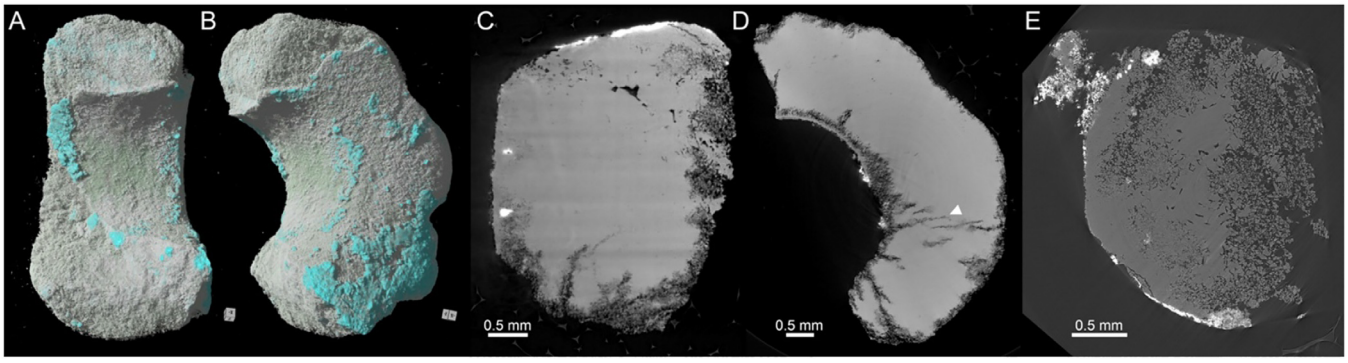

Fig. 4. 3D volume rendering (front, **A** and side, **B**) and virtual sections (**C-D**) through the faience bead sample. Portions of cyan-colored GLZ remains on the sample surface (bright regions in **C**, virtually colored in cyan in **A** and **B**) are identified on the phase-contrast SXCT reconstruction. The bright color indicates a dense (radio-opaque) material composition different from the rest of the sample. The sample's surface is porous and irregular due to surface degradation, with alteration processes interesting the specimen bulk (arrowhead in **D**). **E)** High-resolution detail showing GLZ (bright surface) and high bulk porosity.

ing matter on the BDY edges, identifiable as glazing. In contrast, in the BDY core region, fragments exhibit greater isolation, and are either surrounded by a relatively low-density, highly porous vitreous phase or lacking any discernible vitreous binder.

The outer and inner surfaces of the microbead display a light grey layer with a vitreous aspect attributed to a glazing (GLZ) layer. The external surface of the GLZ is textured with a clear saccharoid appearance, visible in the 3D rendering of Fig. 3A. The glazing layer displays a thickness and a degree of adhesion to the BDY that significantly vary point by point, even within the same CT reconstruction image. The glaze layer is partially not present on the surface, likely as a result of long-term degradation.

Regarding the morphology of the pores, the BDY shows the coexistence of big and rounded pores and small and irregular ones. Cracks in the BDY or involving simultaneously the BDY and the GLZ are detectable. The total porosity of the sample is 17.6 % (Fig. 3C). A significant difference between the porosity of the sample core (24.6 %) and that of the outer layer (6.7 %) demonstrates quantitatively the sealing effect of the surface GLZ (Figs. 3C and D). These microstructural characteristics are in line with the production method known in the literature as efflorescence, based on a mixing paste of quartz grains with glaze [26].

4.2. Faience bead

Fig. 4 presents volume renderings (**A-B**) and virtual sections (**C-D**) through the faience bead. GLZ layers containing copper colorant are visible as bright areas on the sample surface in Fig. 4C and shown in cyan in Fig. 4A-B. The BDY does not show any glaze remains. Additionally, the porous interaction layer (IAL) does not present interstitial glass. These results confirm the production technique as cementation. A gradient in the distribution of microporosity is visible in Fig. 4C and D, with the sample surface being more porous than its core. This is contrary to the microbead (Fig. 3), where a solid GLZ layer surrounds a more porous sample bulk. The presence of porous inclusions with elongated shapes that reach the sample core, visible in Fig. 4C, suggests partial degradation of the sample advancing from the surface. Fig. 4E shows a high-resolution section through one of the bead extremities, where colored GLZ (bright areas on the surface) and high internal porosity attributed to degradation can be seen.

4.3. Egyptian blue

A transverse section through the phase-contrast SXCT reconstruction of Egyptian blue is shown in Fig. 5A. A portion of the bulk material (red box in Fig. 5A) was cropped for further porosity analysis. The measured bulk sample porosity is 19.85 %, with approximately 95 % of the void volume remaining interconnected through the analyzed area. The solid can be described therefore as an open-cell structure. Two distinct types of pores can be identified based on their shape and size: (I) large pores with a regular shape (highlighted by red circles in Fig. 5B) contribute to 4.76 % of the sample porosity and have a diameter of 0.13 ± 0.07 mm (Min.: 0.07 mm, Max.: 1.05 mm, histogram in Fig. 5C). (II) A network of thin, elongated cavities (Thickness: 0.026 ± 0.007 mm, local volume thickness map showed in Fig. 5B) with irregular shape connect large pores and make up for the remaining 15.09 % of the sample porosity. The presence of two different pore types within Egyptian blue is highlighted in the 3D rendering of Fig. 5D.

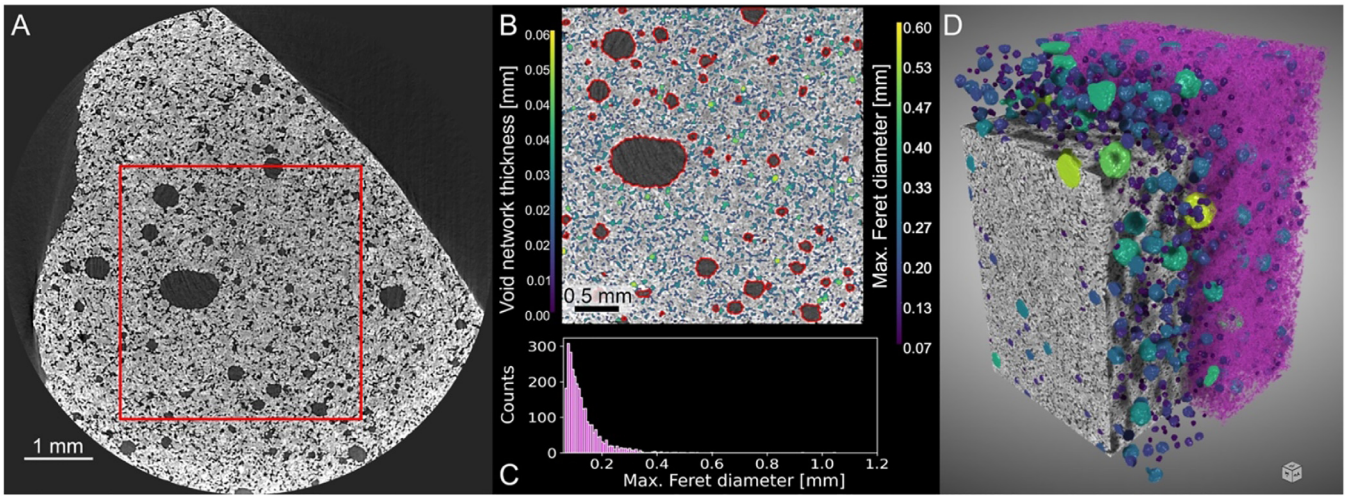

Fig. 5. A) Virtual transverse section through Egyptian blue pigment obtained from phase-contrast SXCT. A portion of the bulk pigment (red box) was selected for porosity analysis. **B)** Detail of the analyzed volume. Large, circular pores (outlined in red) are segmented from the remaining void space with a 3D image opening step. The color overlay shows the local volume thickness of finer cavities. **C)** Size distribution (maximum Feret diameter) of large pores with regular shape. **D)** 3D volume rendering of the analyzed portion of Egyptian blue pigment. Large, regular-shaped pores are colored based on their diameter. A network of thin cavities (magenta) is found to permeate the pigment.

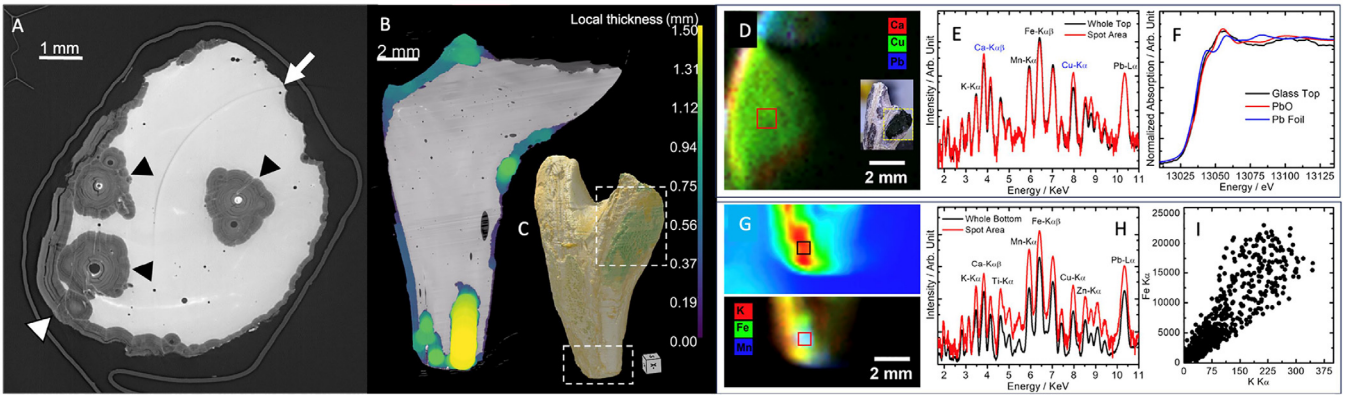

Fig. 6. A) Cross-section through SXCT scan of the Roman glass specimen. Areas of the sample surface with a thick alteration layer and absence of alteration patina (likely due to abrasion) are highlighted by a white arrowhead and arrow, respectively. Pits filled with multi-layer alteration products are highlighted with black arrowheads. **B)** Longitudinal section with color overlay displaying the local thickness of the surface alteration patina. See Suppl. 3 for a detailed description of the patina segmentation and local thickness analysis. **C)** 3D rendering of Roman glass specimen from SXCT. Areas selected for XRF mapping of bulk and altered glass are marked with rectangular boxes. **D)** Overlay of Ca (appearing red), Cu (appearing green), and Pb (appearing blue) chemical distribution from XRF mapping of bulk glass exposed to the sample surface. The spot area selected for local XRF is marked by a red square. **E)** XRF spectra obtained from the whole top of the sample (black line) and spot area (red line). **F)** XANES spectra of the glass top (black line), PbO (red line) and reference Pb foil (blue line) collected in fluorescence and transmission modes around the Pb L3 edge. **G)** Original stack image and overlay of K (modifier shown in red), Fe (colorant agent usually found as impurities in roman glass shown in green), and Mn (colorant agent shown in blue) chemical distribution from XRF mapping of altered glass surface. The spot area selected for local XRF is marked by boxes in the image. **H)** XRF spectra obtained from the whole bottom of the sample (black line) and spot area (red line). **I)** Scatter plot of $K_{K\alpha}$ and $Fe_{K\alpha}$ counts per pixel that manifests the homogenous distribution of K and Fe in the bottom portion.

4.4. Roman glass

Fig. 6 combines the results from phase-contrast SXCT and XRF mapping of the Roman glass. The extent and layered microstructure of surface alteration (white arrowhead) are visible in the SXCT cross-section (Fig. 6A). The unaltered glass bulk is exposed over a limited part of the sample surface (white arrow) which was targeted for XRF mapping. Bulk glass, alteration products, and voids can be identified and segmented owing to their different X-ray attenuation, leading to different intensities in the SXCT images. The porosity of the bulk glass and of the surface alteration layer are 1.32 % and 2.20 %, respectively. The alteration products (patina) account for 25.17 % of the sample volume. Fig. 6B shows a longitudinal section through the sample and results from the local thickness analysis of the surface alteration patina. The patina thickness is 0.67 ± 0.30 mm, with maximum thickness (1.50 mm) found on areas exposed to the sample surface but protected from abrasion by a hollow geometry (alteration pits). Here, a highly organized multi-layer structure (black arrowheads in Fig. 6A) formed as the result of centuries of modification of the silicate glass network is recognizable, as recently observed in [10].

The two ROIs (regions of interest) of the specimen surface selected for XRF and XANES are highlighted by dashed boxes on the 3D SXCT volume rendering of Fig. 6C. Fig. 6 D-F presents the results from analyses performed on ROI 1. This contains a large portion of exposed glass bulk of green color (Fig. 1D and insert in Fig. 6D). Fig 6D shows an RGB tricolor map representing the chemical distribution of calcium (Ca), copper (Cu), and Pb in ROI 1. The complete XRF spectrum of ROI 1 (black line in Fig 6E) shows that the bulk is mainly composed of Ca and Cu. The red line in Fig 6E corresponds to the XRF signal stemming from the bulk spot area indicated with a red box in Fig 6D. The Pb content in the bulk is

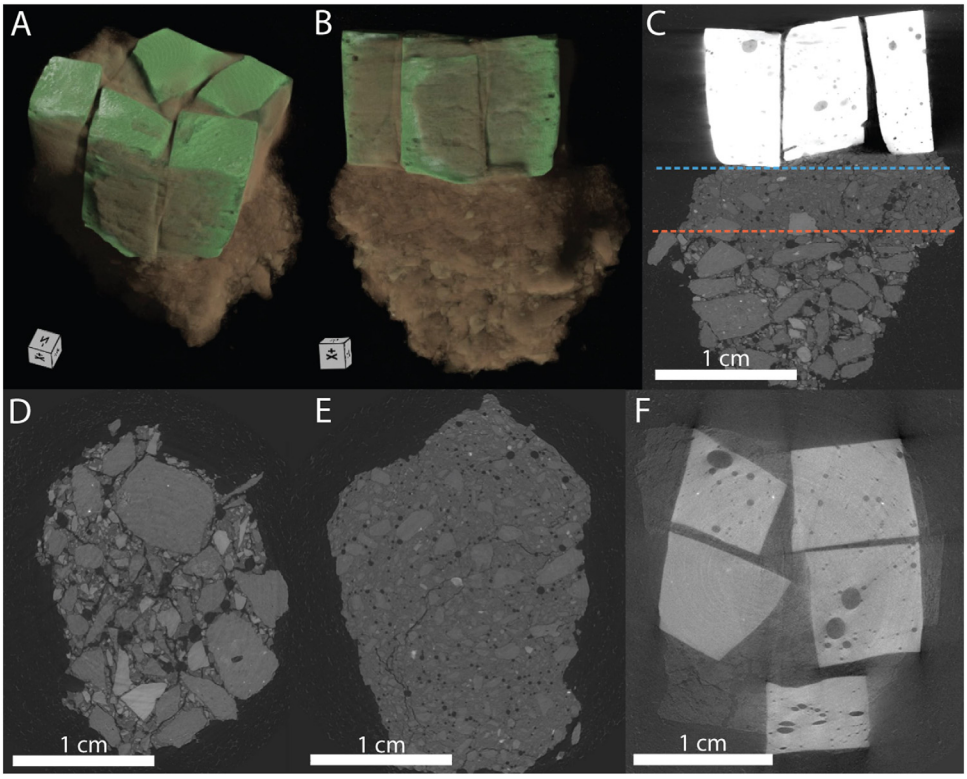

Fig. 7. A-B) 3D renderings showing the top and side of the mosaic replica sample, respectively. The colors used for the visualization are similar to the real ones: green for the tesserae, and brown for the mortar. **C)** Longitudinal section through the sample. Dashed lines indicate the interfaces of the *tesserae*/*Nucleus* stratification (blue) and of the *Nucleus*/*Rudus* stratification (red). **D)** Cross-section of the *Rudus strata* of the specimen, showing prevalent porosity compared to the *Nucleus*, and fractures well aligned with the borders of the aggregates. **E)** Cross-section of compact-appearing *Nucleus strata*. A few thin fractures are visible, along with circular pores within the mortar. **F)** Cross-section of *tesserae strata*. Pores within the glass bulk of the tesserae are visible.

much lower than in the patina (Suppl. 4), indicating Pb contamination from elsewhere. The Pb L3-edge XANES spectra obtained from ROI 1 (Fig. 6F), recorded around 13,035 eV, suggest the existence of Pb in the oxidation state of +2, as it is also found in PbO.

Fig. 6G-I present results obtained from the bottom portion of the sample. The RGB image of Fig. 6G represents the localization of potassium (K), iron (Fe), and manganese (Mn) in the ROI. Fig. 6H shows the XRF spectra obtained from the whole ROI and from the spot area marked by boxes in Fig. 6G, displaying the elemental composition and presence of K, Ca, Mn, Fe, Cu, and Pb as major elements, but also a relative compositional inhomogeneity of the patina. In Fig. 6I the counts of $K_{K\alpha}$ and $Fe_{K\alpha}$ photons per pixel are visualized in a scatter plot. Since this ratio is symmetrically scattered around the bisector and roughly constant, with an increased uncertainty for high count rates, a homogenous distribution of the K and Fe atoms in the bottom portion can be inferred.

4.5. Mosaic mockup

3D renderings (**A-B**) and virtual sections (**C-F**) from SXCT of the Roman mosaic mockup are shown in Fig. 7. The characteristic structure of mosaic samples, with tesserae nested inside the mortar, is visible (Fig. 7A). A longitudinal section through the specimen (Fig. 7C), allows to inspect the mosaic stratification from glass tesserae (top) to the compact mortar beneath and underneath them (Nucleus), and the coarse Rudus mortar characterized by big aggregates (bottom). Colored lines mark the interface between different strata. Moreover, microscopic voids inside the tesserae due to air bubbles trapped inside the glass during the production phase are visible in Fig. 7C, and the cross-section through the tesserae of Fig. 7F. Differences in the composition of the various mortar layers are readily apparent by comparing the cross sections of Fig. 7D-E. The Nucleus mortar (Fig. 7D) is characterized by a fine-grained structure with few pores and thin fractures. Differently, the Rudus mortar (Fig. 7D) shows coarser aggregates and large voids and fractures.

5. Discussion

The characterization of the internal microstructure of unique artifacts is paramount for a comprehensive understanding of their history. SXCT imaging at SESAME BEATS allows studying non-invasively a collection of valuable archaeological specimens with varying size and composition. Hypotheses concerning the manufacturing process of specimens could be verified through a quantitative analysis of the material porosity. This study outlines several examples and protocols for SXCT image reconstruction and processing that can guide cultural heritage specialists in the design of SXCT experiments and in quantitative 3D data analysis tasks. The presented open-source software pipelines provide guidelines for users and can be customized for segmentation and 3D void analysis of diverse materials.

We have demonstrated the possibility to analyze non-destructively faience beads as small as 1 mm, which belong to a class of diminutive, extremely fragile, and unique archaeological objects. A comprehensive qualitative and quantitative insight from SXCT of a collection of faience microbeads is ongoing. Figs. 3 and 4 illustrate the quantification of microstructural information from faience specimens, such as the porosity, distribution, and connectivity of internal and surface phases, which allows us to identify production techniques without reservations. Notably, visualizing with high contrast the distribution of interstitial glass allowed us to differentiate between effloresce and cementation techniques. With this respect, the use of phase-contrast enhancement allows

to obtain detailed volume images that are significant for illuminating ancient technological practices. Compared to SXCT, traditional techniques such as SEM and thin section petrography are limited by a 2D plane of investigation and require sectioning the sample. The possibility to retrieve a volumetric image of the whole sample without damaging it makes SXCT more adequate to pinpoint the distribution of IAL to differentiate between effloresce and cementation techniques, particularly for small and fragile samples [27,28].

The production technique of Egyptian blue is well known. To obtain this pigment, crafts mixed one part lime (calcium oxide, CaO) and one part copper oxide (CuO) with four parts quartz (silica, SiO_2). The result is a heterogeneous material containing quartz, tridymite (a silica polymorph), and cuprorivaite ($CuCaSi_4O_{10}$) [29]. While there is not a definitive recipe, different pigment production mechanisms are possible. Recent research suggests the formation mechanism starts either with CaO or $CaCO_3$, the latter decomposing around 600–700 °C. The production requires O_2 (oxidizing atmosphere) and Cu^{2+} ions to obtain the desired color. In case $CaCO_3$ is used, the heating rate must be controlled, as the CO_2 produced is sensitive to it [30]. The large, regular shape pores identified in our Egyptian blue specimen (Fig. 5) are likely related to the escape of CO_2, suggesting the precursor raw material as $CaCO_3$.

The Roman glass fragment from Petra, Jordan, is the only item in our sample set exhibiting clear signs of surface alteration. Silicate glass corrosion in soil over centuries is an intricate phenomenon that leads to the modification of the glass composition and microstructure. This results in an alteration of the glass' visual appearance, and in microstructural changes putting the sample integrity at risk. Therefore, the motivation for analyzing the material is two-fold. First, the history of the burial environment can be deduced by the chemistry and morphology of alteration layers. Second, it is paramount to quantify the deterioration state of the material. By applying a combination of synchrotron methods (phase-contrast SXCT and XRF), it is possible to quantify non-invasively the local alteration of the glass surface and to pinpoint the material composition of both the bulk material and corrosion patina. XRF allows to identify Pb and Cu as coloring agents present in the glass bulk which give the characteristic dark green color to the material. An elevated presence of Fe in the patina is also found in accordance with other reports [10,31]. In coloring glasses, Cu salts are known to turn glass turquoise ([32] and Henderson 2022), with some copper salts being blue. This fits well into the picture of a deep green glass bulk, that is not necessarily green owing to iron oxides. Iron could be an impurity as it is mainly found in the corrosion layer.

To rationalize further the presence of a corrosion layer on the glass surface, a synchrotron powder X-ray diffraction (XRD) analysis of the soil corresponding to the burial environment of the specimen was performed. XRD can give information related to structure and by that on the phase composition of a sample (e.g., mineral content in case of crystalline constituents). Since XRF cannot access light elements such as C, N, O, or S, XRD is valuable to retrieve information on the matrix of the detected heavy elements. Our analysis (Suppl. 4) reveals a soil composition of around 85% silica, 10% of calcite, and traces of other aluminosilicates and iron oxides. Owing to its carbonate content, the alkaline nature of the soil could have accelerated the leaching of alkali ions from the silica network, favoring the formation of a laminar surface with iridescent layers on the glass surface [33,34].

The image filtering and background removal applied to the Roman glass SXCT dataset facilitated the segmentation task and was required due to the presence of a diffuse image artifact with high background intensity around the sample (Suppl. 3). It might have been possible to segment the glass without preliminary filtering by working on a 32- or 16-bit reconstruction. However, this was not feasible due to the large dataset size. A pipeline for slice-wise image pre-filtering is particularly helpful for large volume datasets generated through detector field of view extension and image stitching, or when the available computing resources are limited.

The Roman mosaic mockup is the object with the largest size analyzed in this study. By extending multiple times the detector's field of view, we have shown that SXCT at SESAME BEATS can be applied to samples several centimeters in size. To scan the selected mosaic piece, the high X-ray attenuation of glass tesserae has to be overcome. The possibility to tune the X-ray beam energy to 70 keV and above makes the technique applicable for relatively dense and large archaeological objects. Our analysis of Roman mosaic allows to visualize the internal microstructure of both mortar and glass within the same experiment. For mosaic conservation and conservation science, this knowledge is fundamental for the individuation of the point of failure of the systems and to see the interconnection of voids and fractures for the inner to the external side of the samples.

6. Conclusions

This study shows the advantages of SXCT and the potential of the technique at the SESAME BEATS beamline for the study of ancient VM by providing examples from a set of different cultural heritage objects. Faience, Egyptian blue, and glass are fragile materials, sensitive to weathering, and tend to easily decompose under diverse climatic conditions. The delicate nature of VM and their unique cultural heritage value urges for their examination through non-destructive and minimally invasive methodologies. In this context, SXCT is increasingly demanded and has become a favorable non-destructive technique for 3D imaging and analysis of cultural heritage artifacts [7].

Our work highlights how high-resolution SXCT phase-contrast imaging can identify and differentiate ancient faience and pigment production technologies, quantify the severity and microstructure of glass corrosion, and assess fracture and mechanical fragility of large artifacts and assemblies such as mosaics.

Notably, computed tomography with synchrotron radiation benefits from the high-photon flux of synchrotron X-ray sources, since high-resolution scans can be performed in a fraction of the time compared to laboratory micro-CT. The contrast of images is significantly improved by the monochromaticity and partial spatial coherence of the X-ray beam. These features make synchrotron facilities adventurous over laboratory micro-CT.

Our work provides for the first time a workflow for SXCT data collection and analysis that can be applied to a broad range of VM and artifacts by experienced synchrotron users as well as researchers who are new to the field. While previous reports provided protocols for SXCT investigations of fossils [35], for virtual histology of archaeological human enamel [36], and for non-invasive assessment of historical instruments [6], this research focuses on a material category not covered so far and on the often-under-discussed topic of 3D image reconstruction and interpretation.

In conclusion, this study displays the importance of the first SXCT facility in Southwest Asia for the non-destructive, high-resolution examination of ancient VM. Non-invasive procedures are particularly vital while working with fragile and valuable artifacts in museums and beyond. The analysis showcased here demonstrates high-quality microstructural information, which is difficult to obtain with lab-based techniques. Combined with other synchrotron analytical modalities (e.g., XAFS, μ-XRD, μ-FTIR, XRDCT [37]), SXCT provides a powerful tool for understanding ancient materials and serves cutting-edge solutions beneficial to archaeolo-

gists, archaeological scientists, as well as conservation and museum specialists.

Acknowledgements

Funding: SESAME provided travel and subsistence support through its user's program. The ID-10 BEATS beamline was funded through the EU's Horizon 2020 Framework Programme, H2020 Excellent Science (grant No. 822535).

Supplementary materials

Supplementary material associated with this article can be found, in the online version, at doi:10.1016/j.culher.2025.01.011.

References

[1] P.J. Withers, C. Bouman, S. Carmignato, V. Cnudde, D. Grimaldi, C.K. Hagen, E. Maire, M. Manley, A. Du Plessis, S.R. Stock, X-ray computed tomography, Nat. Rev. Methods Prim. 1 (2021) 1–21, doi:10.1038/s43586-021-00015-4.
[2] D.J.M. Ngan-Tillard, D.J. Huisman, F. Corbella, A. Van Nass, Over the rainbow? Micro-CT scanning to non-destructively study Roman and early medieval glass bead manufacture, J. Archaeol. Sci. 98 (2018) 7–21, doi:10.1016/j.jas.2018.07.007.
[3] D. Nykonenko, O. Yatsuk, L. Guidorzi, A. Lo Giudice, F. Tansella, L.P. Cesareo, G. Sorrentino, P. Davit, M. Gulmini, A. Re, Glass beads from a Scythian grave on the island of Khortytsia (Zaporizhzhia, Ukraine): insights into bead making through 3D imaging, Herit. Sci. 11 (2023), doi:10.1186/s40494-023-01078-0.
[4] S.P. Rigby, Use of computerised X-ray tomography in the study of the fabrication methods and conservation of ceramics, glass and stone building materials, Heritage 7 (2024) 5687–5722, doi:10.3390/heritage7100268.
[5] M. Cotte, P.-O. Autran, C. Berruyer, C. Dejoie, J. Susini, P. Tafforeau, Cultural and natural heritage at the esrf: looking back and to the future, Synchrotron. Radiat. News 32 (2019) 34–40, doi:10.1080/08940886.2019.1680213.
[6] D. Dreossi, N. Sodini, F. Zanini, Synchrotron radiation microtomography: a tool for the non-invasive structural analysis of historical musical instruments, Synchrotron. Radiat. News 32 (2019) 17–21, doi:10.1080/08940886.2019.1680210.
[7] M.P. Morigi, F. Casali, M. Bettuzzi, R. Brancaccio, V. D'Errico, Application of X-ray computed tomography to cultural heritage diagnostics, Appl. Phys. A 100 (2010) 653–661, doi:10.1007/s00339-010-5648-6.
[8] H. Roemich, F. Zanini, K. Wittstadt, C.M. Weinitschke, N. Sodini, Degradation phenomena on historic glass: non-destructive characterization by synchrotron radiation, Nondestruct. Test. J. 13 (2008) 30–39.
[9] S. Cagno, G. Nuyts, S. Bugani, K.D. Vis, O. Schalm, J. Caen, L. Helfen, M. Cotte, P. Reischig, K. Janssens, Evaluation of manganese-bodies removal in historical stained glass windows via SR-μ-XANES/XRF and SR-μ-CT, J. Anal. At. Spectrom. 26 (2011) 2442–2451, doi:10.1039/C1JA10204D.
[10] G. Franceschin, R. Zanini, G. Iori, E. Longo, G. Divitini, G. Tromba, A. Traviglia, Non-destructive 3D exploration of silicate glass corrosion: a combined multi-scale approach from the macro to the nanoscale, Phys. Chem. Chem. Phys. 26 (2024) 9697–9707, doi:10.1039/D3CP05221D.
[11] R. Zanini, G. Franceschin, L. Vigorelli, G. Iori, L. Chiaberge, E. Longo, L. Guidorzi, A. Re, A.L. Giudice, A. Traviglia, Laboratory and synchrotron X-ray micro–computed tomography to shed light on degradation features of corroded Roman glass, J. Am. Ceram. Soc. (2024) e20241, doi:10.1111/jace.20241.
[12] A. Snigirev, I. Snigireva, V. Kohn, S. Kuznetsov, I. Schelokov, On the possibilities of x-ray phase contrast microimaging by coherent high-energy synchrotron radiation, Rev. Sci. Instrum. 66 (1995) 5486–5492, doi:10.1063/1.1146073.
[13] G. Iori, M. Alzu'bi, A. Abbadi, Y. Al Momani, A.R. Hasoneh, P. Van Vaerenbergh, I. Cudin, et al., BEATS: BEAmline for synchrotron X-ray microTomography at SESAME, J. Synchrotron. Radiat. 31 (5) (2024), doi:10.1107/S1600577524005277.
[14] G. Iori, M. Al Shehab, M. Al-Najdawi, M. Altissimo, I. Cudin, A. Kaprolat, T. Kolodziej, A. Lausi, J. Reyes-Herrera, P. Van Vaerenbergh, Design and ray-tracing of the BEATS beamline of SESAME, in: Presented at the 11th Mechanical Engineering Design of Synchrotron Radiation Equipment and Instrumentation (MEDSI'20), Chicago, IL, USA, 24-29 July 2021, JACOW Publishing, Geneva, Switzerland, 2021, pp. 246–248, doi:10.18429/JACoW-MEDSI2020-WEPA10.
[15] T. Weitkamp, D. Haas, D. Wegrzynek, A. Rack, ANKAphase: software for single-distance phase retrieval from inline X-ray phase-contrast radiographs, J. Synchrotron. Rad. 18 (2011) 617–629, doi:10.1107/S0909049511002895.
[16] D. Gürsoy, F. De Carlo, X. Xiao, C. Jacobsen, TomoPy: a framework for the analysis of synchrotron tomographic data, J. Synchrotron. Rad. 21 (2014) 1188–1193, doi:10.1107/S1600577514013939.
[17] G. Iori, I. Foudeh, M. Alzu'bi, M. Al Mohammad, S. Matalgah, Alrecon: computed tomography reconstruction web application based on Solara, ORE 4 (2024), doi:10.12688/openreseurope.16863.2.
[18] Iori, G., Hans, P., 2025. gianthk/BEATS-CH2024: JCH revisions. https://doi.org/10.5281/zenodo.14592121
[19] D. Paganin, S.C. Mayo, T.E. Gureyev, P.R. Miller, S.W. Wilkins, Simultaneous phase and amplitude extraction from a single defocused image of a homogeneous object, J. Microsc. 206 (2002) 33–40, doi:10.1046/j.1365-2818.2002.01010.x.
[20] P. Cloetens, R. Barrett, J. Baruchel, J.-P. Guigay, M. Schlenker, Phase objects in synchrotron radiation hard X-ray imaging, J. Phys. D: Appl. Phys. 29 (1996) 133–146, doi:10.1088/0022-3727/29/1/023.
[21] N.T. Vo, R.C. Atwood, M. Drakopoulos, Superior techniques for eliminating ring artifacts in X-ray micro-tomography, Opt. Express. 26 (2018) 28396–28412 OE, doi:10.1364/OE.26.028396.
[22] F. Marone, M. Stampanoni, Regridding reconstruction algorithm for real-time tomographic imaging, J. Synchrotron. Rad. 19 (2012) 1029–1037, doi:10.1107/S0909049512032864.
[23] J. Schindelin, I. Arganda-Carreras, E. Frise, V. Kaynig, M. Longair, T. Pietzsch, S. Preibisch, C. Rueden, S. Saalfeld, B. Schmid, J.-Y. Tinevez, D.J. White, V. Hartenstein, K. Eliceiri, P. Tomancak, A. Cardona, Nat. Methods 9 (2012) 676–682.
[24] N. Otsu, A threshold selection method from gray-level histograms, IEEE Trans. Syst. Man Cybern. 9 (1979) 62–66.
[25] M. Harfouche, M. Abdellatief, Y. Momani, A. Abbadi, M. Al Najdawi, M. Al Zoubi, B. Aljamal, et al., Emergence of the first XAFS/XRF beamline in the Middle East: providing studies of elements and their atomic/electronic structure in pluridisciplinary research fields, J. Synchrotron. Radiat. 29 (4) (2022) 1107–1113, doi:10.1107/S1600577522005215.
[26] M.S. Tite, A.J. Shortland, Production Technology of Faiance and Related Early Vitreous Materials, 72, Oxford University School of Archaeology Monograph, Oxford, 2008.
[27] G. Dardeniz, T. Yıldırım, C. Yıldırım, E. Çiftçi, Blue, green, and white faience bead production techniques in the Early Bronze Age central Anatolian site of Resuloğlu (Turkey), Archaeometry 63 (2) (2021) 327–342.
[28] H. Sağlamtimur, G. Dardeniz, E.L. Baysal, Travel of faience beads and metal pins: evidence of long-distance trade in early Bronze Age I (3100–2900 BCE) Başur Höyük, Türkiye, J. Archaeol. Sci.: Reports 52 (2023) 104263, doi:10.1016/j.jasrep.2023.104263.
[29] I. Reiche, E. Chalmin, Synchrotron methods: color in paints and minerals, in: Heinrich D. Holland, Karl K. Turekian (Eds.), Treatise on Geochemistry, 2nd Edition, Elsevier, 2014, pp. 209–239, doi:10.1016/B978-0-08-095975-7.01216-X.
[30] A. Kiss, H.A. Stretz, A. Ueda, R. Mu, Synthesis of Egyptian Blue and mechanisms, J. Phys. Chem. Solids 167 (2022) 110738 ISSN 0022-3697, doi:10.1016/j.jpcs.2022.110738.
[31] E. Burger, D. Rebiscoul, F. Bruguier, M. Jublot, J.E. Lartigue, S. Gin, Impact of iron on nuclear glass alteration in geological repository conditions: a multi-scale approach, Appl. Geochem. 31 (2013) 159–170, doi:10.1016/j.apgeochem.2012.12.016.
[32] with G. Dardeniz, J. Henderson, M. Roe, Primary evidence for glassmaking in Late Bronze Age Alalakh/Tell Atchana (Amuq Valley, Turkey), J. Glass. Stud. 64 (2022) 11–32.
[33] C.M. Jackson, D. Greenfield, L.A. Howie, An assessment of compositional and morphological changes in model archaeological glasses in an acid burial matrix, Archaeometry 54 (3) (2012) 489–507, doi:10.1111/j.1475-4754.2011.00632.x.
[34] S. Toniolo, Soil Characterisation to Investigate the Role of the Burial Environment in Archaeological Glass Alteration, Università Ca' Foscari Venezia, Venice, Italy, 2022 http://dspace.unive.it/handle/10579/21280.
[35] P. Tafforeau, R. Boistel, E. Boller, A. Bravin, M. Brunet, Y. Chaimanee, P. Cloetens, M. Feist, J. Hoszowska, J.-J. Jaeger, R.F. Kay, V. Lazzari, L. Marivaux, A. Nel, C. Nemoz, X. Thibault, P. Vignaud, S. Zabler, Applications of X-ray synchrotron microtomography for non-destructive 3D studies of paleontological specimens, Appl. Phys. A 83 (2006) 195–202, doi:10.1007/s00339-006-3507-2.
[36] A. Nava, P. Mahoney, L. Bondioli, A. Coppa, E. Cristiani, L. Fattore, G. McFarlane, D. Dreossi, L. Mancini, Virtual histology of archaeological human deciduous prenatal enamel through synchrotron X-ray computed microtomography images, J. Synchrotron. Rad. 29 (2022) 247–253, doi:10.1107/S160057752101208X.
[37] E. Possenti, C. Conti, G.D. Gatta, M. Merlini, M. Realini, C. Colombo, Synchrotron radiation μ X-ray diffraction in transmission geometry for investigating the penetration depth of conservation treatments on cultural heritage stone materials, Anal. Methods 12 (2020) 1587, doi:10.1039/D0AY00010H.